The International Journal of Advanced Manufacturing Technology
https://doi.org/10.1007/s00170-024-13411-3

ORIGINAL ARTICLE

Directed energy deposition of PH 13–8 Mo stainless steel: microstructure and mechanical property analysis

Mustafa Kas[1] · Talha Muslim[2] · Oguzhan Yilmaz[1] · Taner Karagoz[2] · Enbiya Turedi[3] · Serap Gumus[3] · Alperen Bayram[2]

Received: 25 August 2023 / Accepted: 10 March 2024
© The Author(s) 2024

Abstract

Laser metal deposition (LMD) is of the directed energy deposition (DED) process which is widely used for producing large-scale, dense, and functional parts in the field of additive manufacturing (AM). This research work investigates the microstructure and mechanical properties of PH 13–8 Mo martensitic stainless-steel parts produced via LMD. The workshop trials were conducted using an LMD system collaborated with a robotic arm to deposit single-track thin walls and horizontal blocks. The microstructural characteristics of the additively manufactured parts were analyzed using an optical microscope. The mechanical properties were evaluated through hardness measurements and uniaxial tensile tests. The influence of energy density and powder deposition density on the characteristic geometry of straight walls was also investigated. The microstructural analysis showed that the microstructure consisted of columnar dendrites that grew epitaxially from the substrate, with primary austenite cells containing intercellular ferrite and martensite laths that were roughly parallel with the retained austenite. When the energy density increased from 43 to 86 J/mm^2 (a doubling of energy density), there was an increase in secondary dendritic arm spacing (SDAS) by approximately 250% in the first layer and approximately 90% in the top layer. The difference in SDAS change between the first and top layers can be attributed to the difference in cooling rates experienced by each layer during the additive manufacturing process. Increasing powder deposition density from 0.5 to 1 g/min results in a decrease in porosity from 3% to less than 1% and an increase in strength from 800 to over 1000 MPa. The hardness of the deposits was found to range from 300 to 400 HV. This variation in hardness can be attributed to differences in microstructure resulting from changes in cooling rates at different heights.

Keywords Additive manufacturing (AM) · Laser metal deposition (LMD) · Microstructure · Mechanical properties · PH 13–8 Mo stainless steel

✉ Mustafa Kas
mustafakas@gazi.edu.tr

Talha Muslim
tmuslim@coskunoz.com.tr

Oguzhan Yilmaz
oguzhanyilmaz@gazi.edu.tr

Taner Karagoz
TKARAGOZ@coskunoz.com.tr

Enbiya Turedi
enbiya.turedi@kocaeli.edu.tr

Serap Gumus
sgumus@kocaeli.edu.tr

Alperen Bayram
abayram@coskunoz.com.tr

[1] Advanced Manufacturing Technologies Research Group (AMTRG), Faculty of Engineering, Gazi University, 06570 Maltepe, Ankara, Turkey

[2] Coşkunöz Holding R&D Center, Fethiye OSB Mh. Sari Cd. No: 1, 16140 Bursa, Turkey

[3] Department of Metallurgical and Materials Science and Engineering, Kocaeli University, 41380 Izmit, Kocaeli, Turkey

Published online: 14 March 2024

1 Introduction

Additive manufacturing (AM) technologies have revolutionized the manufacturing industry, ushering in the fourth industrial revolution. These processes provide many advantages over traditional manufacturing techniques, such as the ability to produce complex shapes [1], reducing production lead time, and eliminating the need for expensive tooling [2]. Several industries, including aerospace, automotive, defense, healthcare, and die-mold tooling, use AM technologies. Powder bed fusion (PBF) and directed energy deposition (DED) processes are the most commonly used AM techniques to manufacture metallic components. Both PBF and DED have great potential for producing functional and customized metallic parts for various applications. However, DED has many advantages over PBF such as higher deposition rate, low material waste, repairing of coexisting parts, creation of heterogeneous components, low operation cost, and does not require a vacuum chamber or an inert gas environment [3].

Laser metal deposition (LMD) is a type of DED technique that uses a high-power laser beam to melt and fuse metal powders on a substrate or previously deposited layers. LMD produces functional metal parts with customized properties and complex geometries that are challenging to achieve with conventional methods. The process is controlled by a computer-aided design (CAD) model that guides the laser beam and the motion system to create the desired shape layer by layer. LMD has many applications, such as the repair and remanufacturing of high-value parts [4], printing functionally graded materials (FGM) [5–7], surface coating of parts exposed to harsh conditions or heavy loads [2], and manufacturing near net-shaped components [8]. The ability of LMD to repair and extend the useful life of parts, decrease environmental impact, and generate significant economic benefits related to part repair is driving its increasing use in industrial applications [9]. LMD has been used to deposit various materials, including titanium [10], Inconel [11], aluminum [12], steel [13], and copper [14].

Precipitation-hardening stainless steels (PH SS) are widely used in applications requiring high strength, excellent corrosion resistance, and good ductility [15]. Chromium content provides corrosion resistance, while intermetallic phases of alloying elements, such as aluminum, titanium, niobium, and copper, obtained through precipitation hardening heat treatment, offer high strength [16]. PH SS can be categorized into three groups based on their microstructure, namely martensitic, semi-austenitic, and austenitic [17].

Martensitic PH SS grades are classified as high- or low-carbon steels with a chromium content of 12 to 17%. As martensitic PH SS solidifies, the δ-ferrite converts to austenite upon cooling, which then transforms to martensite at room temperature. Due to their low carbon content, martensitic PH SS has a softer martensitic structure than other martensitic steels [18]. Commercially available martensitic PH SS grades include PH 13–8 Mo, 17–4 PH, and 15–5 PH where the first and second numbers represent the content of the main alloying elements, Cr and Ni [19]. PH 13–8 Mo is particularly useful for applications requiring both strength and toughness [20] as well as good corrosion resistance [21], such as valve parts, fittings, aircraft components, petrochemical applications [22], and safety and security components [23]. It is hardened by the precipitation of β-NiAl precipitates when precipitation hardening is applied [24]. In comparison to the other martensitic PH SS grades, PH 13–8 Mo has the highest combination of corrosion resistance, strength, and toughness, making it the material of choice for operations in extreme environmental conditions [23]. Conventional machining processes find it challenging to manufacture PH SS parts due to their high strength and hardness. AM technologies can provide an alternative solution for the manufacturing of PH SS parts [25].

Combining PH SS with AM has the potential to create a new class of high-strength, high-performance parts that are both efficient and cost-effective to produce. By controlling the microstructure of the steel at the additive manufacturing stage, it is possible to tailor the properties of the final part. Adeyemi et al. [26] found that the quantity of δ-ferrite increased with the laser power during laser metal deposition (LMD) of 17–4 PH SS, while Vendra et al. [27] demonstrated that heat treatment significantly influenced the fatigue performance and mechanical properties of LMD-fabricated 17–4 PH SS. Similarly, Yu et al. [28] investigated the effect of laser remelting (LR) processing on the microstructure and mechanical properties of laser-deposited 17–4 PH SS. Besides LMD, other AM techniques such as wire-based AM and powder bed fusion have also been explored to process 17–4 PH SS [29–36]. Aripin et al. investigated the effects of different building orientations and post-fabrication heat treatment (solution annealing and aging) on the mechanical and microstructural characteristics of PH 17–4 SS samples fabricated by selective laser melting (SLM) [37]. In another study by Bandar and Yang [38], the microstructure and mechanical properties of 17–4 PH SS were investigated using micropillar compression testing and transmission electron microscopy (TEM). The authors concluded that the microstructures and properties of 17–4 stainless steel specimens fabricated by DMLS vary significantly from those of specimens produced using conventional methods. They also suggested that the DMLS process can be optimized by controlling the heat treatment parameters to achieve the desired properties. In contrast, only limited studies are available in the literature on the AM of PH 13–8 Mo SS. Ghaffari et al. [21]

investigated wire-based AM and found that it could produce high-quality components with desirable mechanical properties and microstructures, demonstrating the potential of fabricating PH 13–8 Mo martensitic SS parts with comparable hardness and tensile strength to parts fabricated with other methods. Sanjari et al. studied the effect of build orientation on the grain structure of PH 13–8 Mo alloy processed by selective laser melting (SLM), finding that changing the build orientation from horizontal to vertical affects microstructural features such as phase fraction, grain size, and grain morphology [39]. Turnier et al. compared the structure and mechanical properties of laser powder bed fused and wrought PH 13–8 Mo SS, revealing statistically significant differences in yield strength, UTS, and ductility between the samples produced through LMD and wrought samples, but no significant differences in elastic moduli [40]. Zhang et al. investigated the effect of process parameters and heat treatments on the properties of SLM-processed PH 13–8 Mo alloy, observing that the tensile strength increased significantly after heat treatment [41]. Asgari and Mohammadi used direct metal laser sintering to manufacture CX alloy, a corrosion-resistant and high-strength alloy, and reported high ultimate tensile strength and good elongation to fracture, indicating outstanding tensile properties at horizontally built samples [42]. Nemani et al. investigated the microstructure and corrosion characteristics of PH 13–8 Mo martensitic stainless steel alloy fabricated by wire arc additive manufacturing (WAAM). The authors showed how the alloy changed after being subjected to solution and aging treatments at different temperatures [43]. Zheng et al. examined the microstructure of PH 13–8 Mo steel fabricated via LMD and found that ductility decreased due to unmelted powder particles and porosity [23]. Muslim et al. investigated the effect of energy density on the geometry of laser deposited PH 13–8 Mo steel, finding that low-energy density resulted in either no or poor deposits, while high-energy density resulted in improper deposits due to heat buildup [44].

In this study, we focus on investigating the feasibility of using LMD as a processing method for PH 13–8 Mo SS. We conduct experiments using an LMD system with a robotic arm to deposit single-track thin walls and horizontal blocks and investigate the microstructure and mechanical properties of the additively manufactured parts. Specifically, we analyze the influence of energy density and powder deposition density on the characteristic geometry of straight walls. The microstructural characteristics of the additively manufactured parts are analyzed using an optical microscope, while the mechanical properties are evaluated through hardness measurements and uniaxial tensile tests. Finally, we compare the as-built mechanical properties of the laser-deposited PH 13–8 Mo with those obtained using other AM techniques. This study contributes to the limited literature available on the processing of PH 13–8 Mo using LMD processes and provides insights into the feasibility of this technique for PH 13–8 Mo.

2 Materials and methods

2.1 Feedstock powder

The powder material used in this study was PH 13–8 Mo stainless steel supplied by Sandvik Osprey Ltd, UK. The powder was gas-atomized and had a particle size range of 45–150 µm. The chemical composition of the powder is shown in Table 1.

2.2 LMD system setup and experimental details

The LMD experiments were performed using an Erlaser Hard + Clad machine developed at Erlas, Germany. The experimental setup as shown in Fig. 1 consists of a water-cooled coaxial discrete powder nozzle attached to a 6-axis industrial robot (Kuka Kr 90). The robot is mounted on a linear table with a working range of 4 m. The laser source is a fiber-coupled high-power diode laser (Laserline LDF 4000 – 100) with a wavelength of 900 to 1080 nm and a maximum power of 4.0 kW. The fiber diameter is 1.0 mm, and the laser spot size is fixed at 3.5 mm. Argon is used as both a carrier gas and a shielding gas to transport the powder from the hopper to the nozzle and to prevent oxidation, respectively.

2.2.1 Straight wall deposition

To determine the optimal process parameters for LMD of PH 13–8 Mo, twenty-five trial experiments were conducted with different combinations of laser power, scan velocity, and powder feed rate. Based on the analysis of the deposits, the process parameter ranges were defined as follows: laser power of 1200–1800 W, scan velocity of 6–8 mm/s, and powder feed rate of 3.5–4.5 rev/min. The shielding gas flow rate was kept constant at 7 L/min throughout the experiments. Table 2. shows the process parameter combinations used for straight wall depositions.

For each set of process parameters, a 30-mm-long straight wall with ten layers was deposited. The interlayer height was 1 mm, and the tool path was unidirectional. To study the effect of cooling time on the microstructure, a delay time

Table 1 Chemical composition of the PH 13–8 Mo powder (wt %)

Cr	Ni	Mo	Al	Mn	Si	C	Fe
11.8	9.3	1.56	1.43	0.3	0.19	0.017	Balance

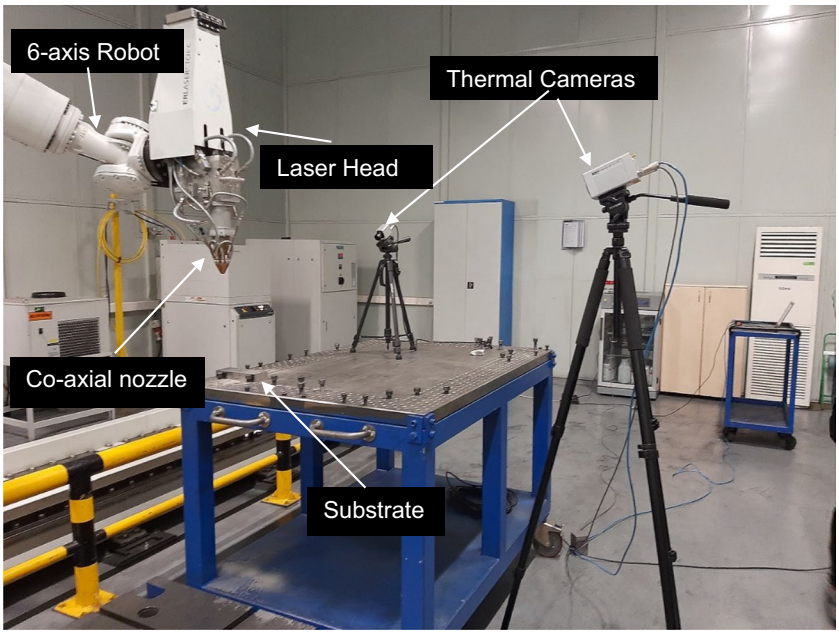

Fig. 1 The manufacturing setup and the equipment used for LMD of PH 13–8 Mo straight walls and block

Table 2 Process parameter combinations for laser metal deposition of PH 13–8 Mo straight wall geometries

Sample no	Laser power (*W*)	Scan velocity (mm/s)	Powder flow rate (rev/min)	Gas flow rate (l/min)	Energy density (J/mm^2)	Powder deposition density (gram/mm^2)
1	1200	6	3.50	7	57.14	0.0090
2	1200	7	4.00	7	48.98	0.0088
3	1200	8	4.50	7	42.85	0.0087
4	1500	6	4.00	7	71.42	0.0103
5	1500	7	4.50	7	61.22	0.0099
6	1500	8	3.50	7	53.57	0.0067
7	1800	6	4.50	7	85.71	0.0115
8	1800	7	3.50	7	73.46	0.0077
9	1800	8	4.00	7	64.28	0.0077

of 1.5 and 3 min was applied after the third and the sixth layers, respectively. The delay time was determined based on the authors' previous studies. The substrate material was 1050 stainless steel with a thickness of 30 mm. The heights and widths of the straight walls were measured at three equidistant points on ImageJ software. The numerical data collected was averaged out for each of the straight walls. The deposits were cut into three subsections at 10-mm intervals using wire electrical discharge machining (WEDM), with 15 mm of the substrate attached to each subsection. The middle subsection was used for microstructural analysis, as shown in Fig. 2.

The quality of the deposited geometry depends on the critical process parameters such as laser power, scan velocity, and powder feeding rate. These parameters affect the amount of energy and material delivered to the melt pool during the LMD process 1. Therefore, two combined parameters are defined to analyze their influence: energy density (ED) and powder deposition density (PDD). ED is the ratio of laser power to scan velocity and laser beam diameter, and it represents the energy input per unit area of the melt pool. ED can be calculated as follows [45]:

$$ED\left(J/mm^2\right) = P/vD \tag{1}$$

ED must be within an optimal range to achieve a good fusion bond between layers. If ED is too high, it can cause excessive dilution of the substrate material. If ED is too low, it can result in insufficient melting of the substrate and the powder. PDD is the ratio of powder feeding rate to scan velocity and laser beam diameter, and it represents the mass of powder deposited per unit area of the melt pool. PDD can be calculated as follows [46]:

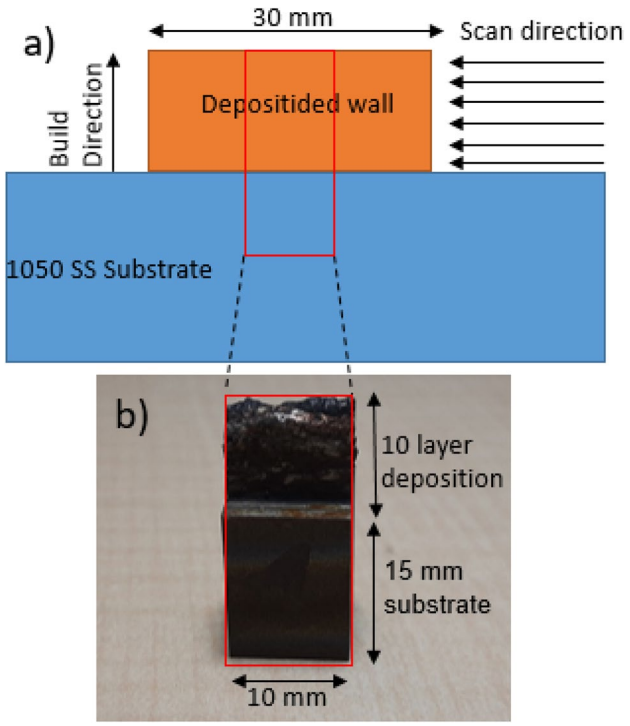

Fig. 2 **a** Schematic of straight wall fabricated via LMD, **b** subtracted mid-section of straight wall for microstructure analysis

$$PDD\left(g/mm^2\right) = G/vD \tag{2}$$

where G is the powder feeding rate (g/s), v is the scan velocity (mm/s), and D is the laser beam diameter. In this study, we report only the effects of the combined parameters ED/PDD on the LMD of PH 13–8 Mo. The aim was to understand how this material behaves under different LMD conditions. LMD is a highly nonlinear process with complex interactions between individual process parameters.

2.2.2 Horizontal block deposition

To evaluate the mechanical properties of the LMD PH 13–8 Mo, a horizontal block with 25 layers was deposited on a 30-mm-thick 1050 stainless steel substrate. The block dimensions were 130 mm in length and 180 mm in width. Process parameters are as follows: laser power of 1500 W, scan velocity of 8 mm/s, powder feed rate of 3.5 rev/min, and shield gas flow rate of 7 l/min. A zig-zag tool path strategy was adopted. The block and the schematic diagram of the deposition are shown in Fig. 3a. From the block, eight sub-sized tensile coupons (ASTM E8) were extracted using wire electrical discharge machining (WEDM). The tensile coupons had a thickness of 3 mm, and the gauge length was 50 mm with a cross-sectional area of 6.25 mm^2. The coupons and their locations in the block are shown in Fig. 3.

2.3 Mechanical and microstructural characterization

The microstructure in the middle subsections of the straight walls was examined using an Olympus BX41 optical microscope. Before the microstructural investigation, the samples were ground using SiC abrasive papers of 320–1200 grit size roughness cloth polished using a 3-µm diamond suspension applied on polishing cloths and etched with Fry's etchant (30 ml H2O, 40 ml HCl, 25 ml ethanol, 5 g CuCl2). The hardness was measured using a Future-tech FV-100 Vickers hardness tester at three points on each layer of the straight walls and then averaged out. The load applied was 500 g, and the dwell time was 15 s. Uniaxial tensile tests were performed on the Instron 5989-L3619 tensile test device at the strain rate of 2 mm/min. The tests were performed at the ambient temperature of 21 °C. The load and displacement data were recorded by the device software and used to calculate the stress–strain curves. The yield strength, ultimate tensile strength, and elongation at fracture were determined using the 0.2% offset rule.

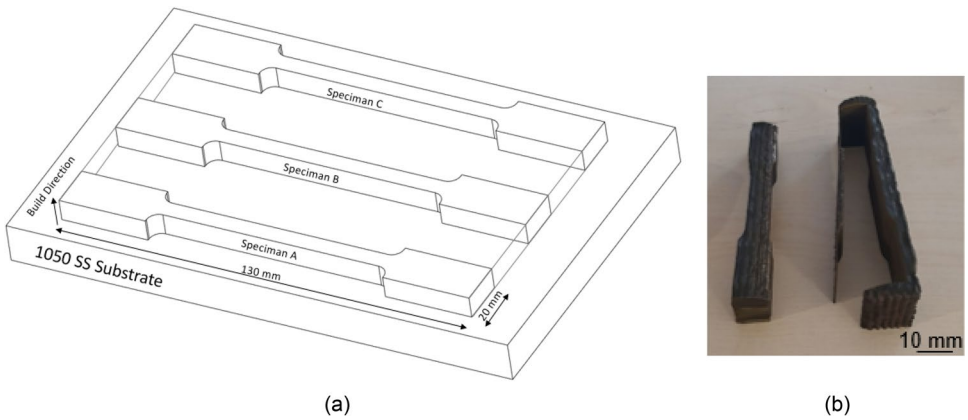

Fig. 3 **a** Schematic of the block manufactured via LMD, **b** tensile specimens extracted from the block

3 Results and discussions

3.1 Geometric characterization

The geometrical characteristics of the straight walls were influenced by the ED and the PDD, as shown in Fig. 4. The figure displays the variation of each geometrical variable with respect to ED and PDD on multi-axis graphs. The data points were fitted with a surface using MATLAB software®.

The central height of the straight walls increased with both ED and PDD, as shown in Fig. 4a, b. The increase in central height was due to higher ED providing more energy to melt the powder particles, and higher PDD delivering more powder particles to the melt pool region, resulting in more material being deposited. As a result, more material was deposited, and the central height of the walls increased. The central height of the straight walls has experienced a significant increase at ED of 54 J/mm^2 and a PDD of 0.06 g/mm^2, the height was measured at 6.4 mm. However, with an increased ED of 71 J/mm^2 (1.3 times higher) and a higher

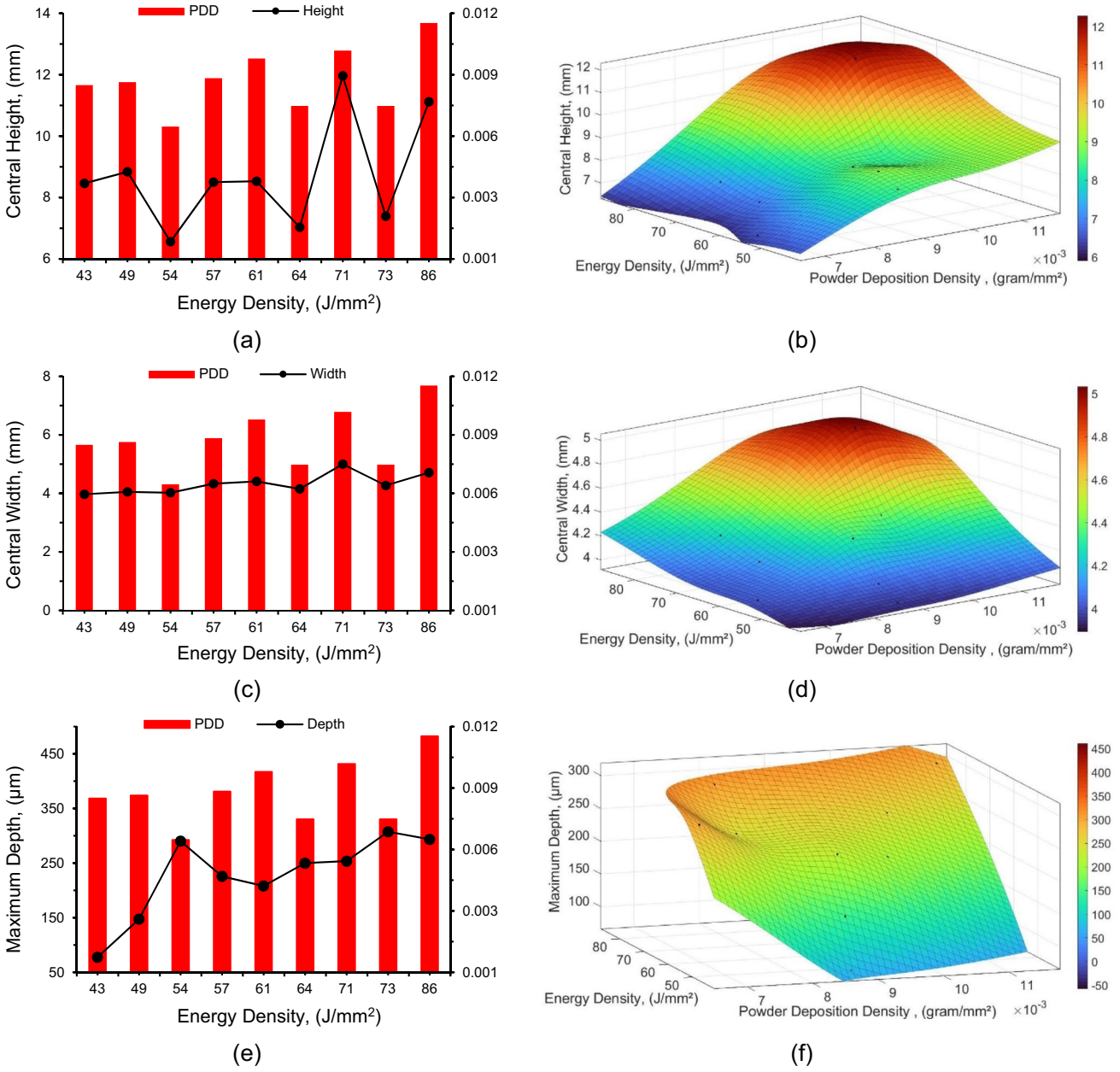

Fig. 4 Geometric characteristics of straight wall deposits. **a**, **b** Central height vs ED & PDD; **c**, **d** central width vs ED & PDD; **e**, **f** maximum depth vs ED & PDD

PDD of 0.1 g/mm^2 (1.7 times higher), the height doubled to 12 mm. Similarly, when the ED rose by 1.5 times to 86 J/mm^2 and the PDD increased by 1.2 times to 0.11 g/mm^2, the wall height grew from 8.5 to 13.2 mm. In this case, it can be observed that the increase in ED was more pronounced than the increase in PDD. Consequently, the growth rate of the wall height was reduced from 2 to 1.3 times. This analysis demonstrates that the effect of PDD on wall height is more dominant compared to ED. While the increase in ED has progressed from 1.3 to 1.5 times, the rise in PDD has decreased from 1.7 to 1.3 times. Consequently, the overall impact on wall height has diminished from doubling to 1.3 times. In summary, these findings highlight the significant influence of PDD in determining wall height, surpassing the effects of ED. However, there was a limit to how much PDD could increase the height, as too high PDD could lead to unmelted powder particles and lower material utilization. This could affect the buy-to-fly ratio, which is important for aerospace applications [47]. The central height ranges from 6.56 to 11.96 mm. Figure 4a shows also some jumps in the height at 71.42 J/mm^2 as PDD increased. Similar jumps were observed at other ED levels as well. Figure 4b shows that the increase in height was more pronounced at higher ED levels when PDD increased.

The central width of the straight walls also increased with both ED and PDD, as shown in Fig. 4c, d. This was because higher ED increased the energy per unit area and thus enlarged the melt pool width [48] which determined the width of the deposit. Higher PDD also contributed to a wider deposit by delivering more material to the melt pool region. The maximum width, as depicted in Fig. 4d, was observed at the combination of the highest values of ED and PDD. Specifically, the central width of the straight wall increased from 1 mm at 35 J/mm^2 ED and 0.1 g/mm^2 PDD to 3 mm at 100 J/mm^2 ED and 0.3 g/mm^2 PDD. The increase in central width was more pronounced at higher ED levels when PDD increased. The laser spot diameter might also influence the width of the single-track multilayer deposit. The average width ranged from 3.97 to 5.00 mm.

Figure 4e, f shows the variation of the melt pool penetration depth with ED and PDD. The melt pool depth ranged from 77.53 to 307.5 µm. Higher ED increased the substrate temperature and thus increased the melt pool penetration depth below the substrate. Higher PDD reduced the ED incident on the substrate by increasing the laser-powder interaction in the air. This resulted in a lower melt pool penetration depth below the substrate. The minimum melt pool penetration depth was observed at low ED and high PDD, as shown in Fig. 4f. The maximum melt pool penetration depth was observed at high ED and low PDD, as shown in Fig. 4f. The maximum depth of the straight wall exhibited a decrease from 0.3 to 0.2 mm when comparing different combinations of ED and PDD values. Specifically, at an ED of 54 J/mm^2 and a PDD of 0.008 g/mm^2, the maximum depth was measured at 0.3 mm. However, with an increased ED of 61 J/mm^2 and a higher PDD of 0.1 g/mm^2, the maximum depth decreased to 0.2 mm. This trend suggests that as the PDD parameter increased beyond certain thresholds, there was a notable decrease in the maximum depth of the straight wall. In other words, higher PDD values had a diminishing effect on the ED. These findings highlight the inverse relationship between PDD and the ED. Increasing PDD beyond certain thresholds led to a decrease in the maximum depth, indicating that the impact of PDD on the depth is significant.

3.2 Porosity analysis

Porosity is a common defect observed in additively manufactured parts, particularly in powder-fed processes. The presence of porosities in the deposited material can be attributed to unmelted powder particles or entrapped gas within the melt pool region. Porosity originating from the feedstock powder can be caused by the presence of satellites and irregularly shaped powder particles. Unmelted powder particles result in a lack of fusion (LOF) defects, occurring when there is insufficient energy to fully melt the powder particles [49, 50]. LOF porosity is typically found at the interfacial boundaries of each track or layer [2] and the neighboring deposited tracks [51]. These porosities exhibit sharp edges and irregular shapes [52], leading to the development of high local stresses [2]. Proper adjustment of energy density (ED) and overlap percentage can help minimize LOF porosity.

In the case of the laser metal deposition (LMD) process, a carrier gas, commonly argon, is utilized to deliver the powder to the melt region. Additionally, a shielding gas, also typically argon, is employed to protect the melt pool region from oxidation. During the process, gas bubbles can become trapped within the melt, resulting in gas porosity. Gas porosities are spherical in shape, occur within layers, and do not form at fixed locations [2]. Porosity originating from the feedstock is reported as a potential source of porosity within the layers during the LMD process [53, 54]. The presence of porosity is undesirable as it reduces material properties [55]. Pores can lead to the formation of small cracks, diminishing the material's ability to conduct heat effectively [56], while also decreasing the fatigue life due to acting as stress concentration sites [57].

Figure 5a, b illustrates the fluctuation of cross-sectional porosity levels (%) in relation to ED and powder deposition density (PDD). Figure 5a demonstrates that cross-sectional porosity is influenced by both ED and PDD. Notably, Fig. 5b reveals that the highest cross-sectional porosity occurs at high ED and low PDD. This behavior can be attributed to the presence of convective fluid flow within the melt pool, known as the Marangoni flow. The Marangoni flow arises from surface tension gradients, driving surface flows from

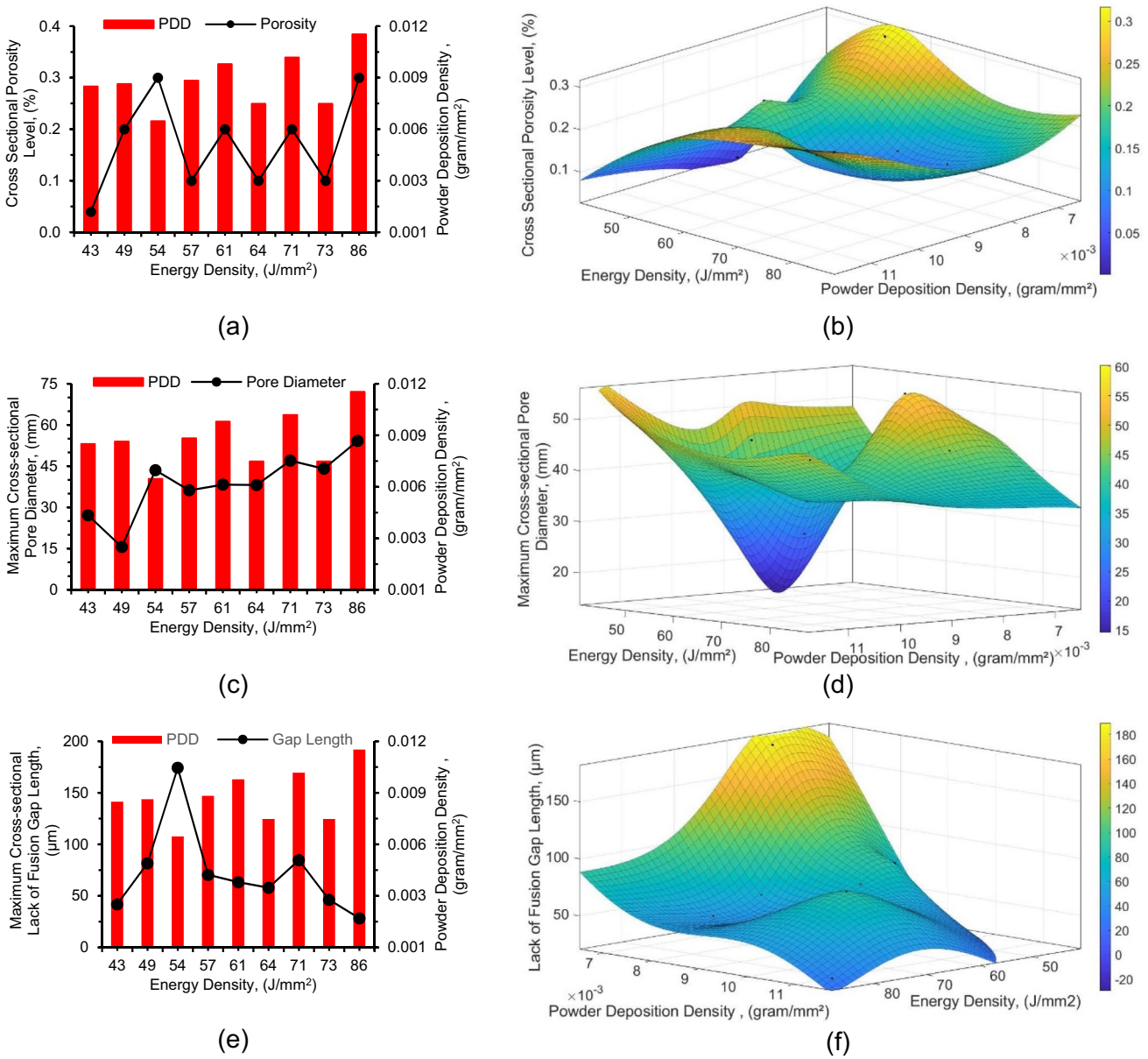

Fig. 5 **a**, **b** Cross-sectional porosity vs energy density and powder deposition density; **c**, **d** maximum pore diameter vs energy density and powder deposition density; **e**, **f** maximum gap length vs energy density and powder deposition density

regions of low-surface tension to those of high-surface tension under the thermocapillary force [58]. The dynamics of the flow in the melt pool region intensify with increasing ED. As a result, the Marangoni flow tends to retain more entrapped gas bubbles. The flow drags these gas bubbles toward the bottom of the melt pool, where they become trapped upon solidification, leading to increased gas porosity. Additionally, the evaporation of material at high ED also contributes to pore formation [59]. The rotational flow facilitates the collision and coalescence of gas bubbles, resulting in the formation of larger pores [60]. It is worth noting that gas porosity can also be observed at low ED, where the high solidification rates entrap gas bubbles before they can escape, thus causing porosity [49, 61].

Figure 5c, d illustrates the variations in cross-sectional maximum pore diameter in relation to ED and PDD. Figure 5c shows that the lowest maximum pore diameter, measuring 15.61 μm, occurs at low ED/PDD values (48.98 J/mm^2, 0.0087 g/mm^2). Conversely, the highest maximum pore diameter is observed at high ED and PDD (85.71 J/mm^2, 0.0035 g/mm^2). The pore diameter ranges from 15.61 to 54.19 μm in all deposited samples. The spherical gas porosities can be visualized in Figs. 6 and 7a in the subsequent sections.

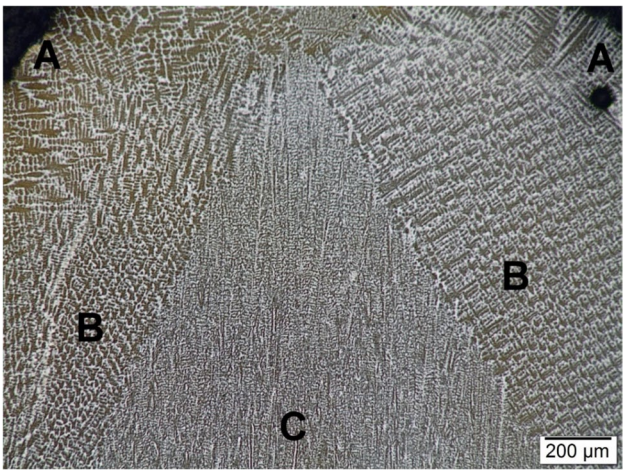

Fig. 6 Microstructural image showing adjacent columnar (**A**), cellular (**B**), and fine (**C**) dendritic top-layer regions in etched sample 3 (1200 W, 8 mm/s, 4.5 rev/min, bottom)

Figure 5e, f depicts the changes in the cross-sectional maximum lack of fusion (LOF) gap length in relation to ED and PDD. The maximum LOF gap length is observed at low ED and PDD values (53.57 J/mm^2, 0.0020 g/mm^2) as shown in Fig. 5f. Figure 5f further illustrates that, at a constant PDD, increasing ED leads to a decrease in the LOF gap length. The lowest LOF gap length is observed at the highest ED and PDD values (85.71 J/mm^2, 0.0035 g/mm^2). The LOF gap lengths range from 28.27 to 174.34 µm across all deposited samples.

3.3 Microstructural characterization

In metal additive manufacturing processes, solidification commonly occurs at a high rate and occurs in the direction of heat transfer, with molten metal crystals growing in the same direction. Conduction and convection are the primary modes of heat transfer in the additive manufacturing process. Conduction, which occurs within the melt pool during deposition, is the most influential mode of heat transfer in LMD. Heat dissipates from the hot region to the cold region during solidification.

The macro-structural morphology of the laser-deposited PH 13–8 Mo is determined by grains with columnar, cellular, and fine dendritic solidification patterns, as depicted in Fig. 6. At low-energy density and high-powder deposition density, the grains were fine and equiaxed, indicating a rapid solidification and nucleation process. At high-energy density and low-powder deposition density, the grains were coarse and columnar, indicating a slower solidification and growth process. Following inoculation using Ni-based heterogeneous nuclei, the formation of columnar grains is effectively hindered, thus triggering a transition from columnar to equiaxed microstructure as shown in Fig. 6, region C. In this transformed microstructure, equiaxed crystals prevail, and their size undergoes a gradual coarsening along the solidification direction. Equiaxed crystals exhibit a greater degree of diversity compared to columnar grains and lack discernible directional alignment at the central region. According to the Hall–Petch theory, the presence of a refined equiaxed grain structure exerts a pronounced influence on enhancing the yield strength of the alloy. Moreover, the abundance of grain boundaries in this microstructure facilitates material deformation processes [62].

Columnar grains spanning multiple layers started to form due to epitaxial grain growth at the bottom as shown in Fig. 6, A and B regions. The solidification process begins at the solid–liquid interface, such as the interface between the melt pool and the substrate or between the melt pool and the previously deposited layers [63]. Crystals develop at these interfaces, acting as nucleation sites. As solidification progresses, the crystals nucleated on the substrate or previously deposited layers grow in size. In the initial stage of solidification, competitive growth of primary δ-ferrite grains occurs for the first layer. The growth direction of these grains < 100 > matches the heat dissipation direction, with grains aligned in this direction having a higher chance of growth compared to those with less favorable

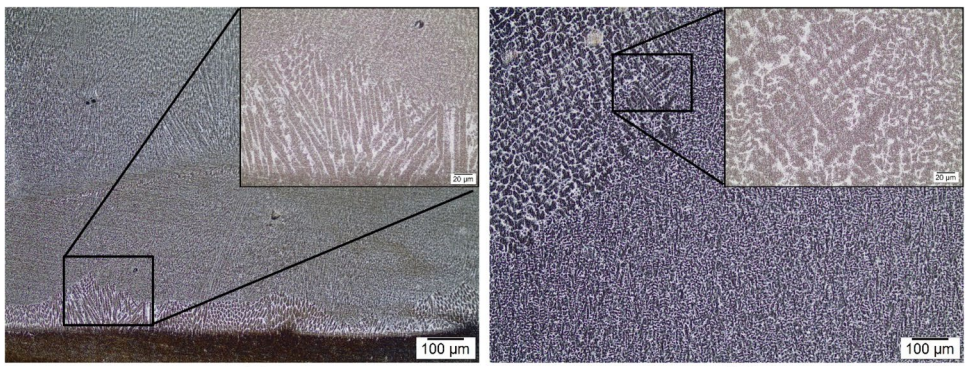

Fig. 7 Selected OM images of the microstructure of the PH 13–8 Mo stainless steel specimens exposed at the lowest which is located in the bottom layer (**a**) and the highest which is located in the top layer (**b**) LD level of 42.85 and 85.71 J/mm^2, respectively

crystallographic orientation. With subsequent layers, the crystals follow the crystallographic orientation of the previous layer, resulting in epitaxial growth. This growth mechanism leads to a reduction in the number of grains and an increase in their size, resulting in coarse columnar grains [64]. The microstructure of the PH 13–8 Mo at the bottom where near the substrate consists of columnar dendrites growing epitaxially from the substrate and primary austenite cells containing intercellular ferrite. Additionally, martensite laths nearly parallel to the retained austenite can be observed. The dominant microstructure of additively manufactured PH 13–8 Mo at room temperature is characterized by δ-ferrite embedded in a low-carbon martensite matrix.

The phase transformation sequence for martensitic PH stainless steel is as follows:

$$\begin{aligned}\text{liquid(L)} \rightarrow \text{L} + \delta - \text{ferrite} \rightarrow \delta - \text{ferrite} \rightarrow \delta - \text{ferrite} \\ + \gamma \rightarrow \delta - \text{ferrite} + \gamma + \text{M} \rightarrow \delta - \text{ferrite} + \text{M}\end{aligned} \quad (3)$$

Two solid-state transformations are involved in the cooling process of the martensitic PH SS. The cooling process of martensitic PH stainless steel involves two solid-state transformations: shear transformation (austenite to martensite) [65] and diffusion-controlled transformation (δ-ferrite to austenite) [66]. The fast cooling rate and on-equilibrium nature of additive manufacturing restrain the transformation of δ-ferrite to austenite. Consequently, a considerable amount of untransformed δ-ferrite phase remains in the martensitic matrix at room temperature [67]. Consequently, a considerable amount of untransformed δ-ferrite phase remains in the martensitic matrix at room temperature [21].

High cooling rates can result in a larger volume fraction of δ-ferrite at room temperature because of the restricted diffusional transformation of δ-ferrite to austenite. For low cooling rates, there is sufficient time for the diffusional transformation of δ-ferrite to austenite, decreasing the amount of δ-ferrite at room temperature [65].

Figure 7 shows selected optical microscope images of the microstructure of PH 13–8 Mo stainless steel specimens exposed to the lowest and the highest energy densities (ED) during the LMD process. These images reveal the differences in microstructure at different ED levels.

NiAl precipitates, which can be up to 7 nm in diameter, may exist in the as-built conditions but are not detectable through light microscopy. This can be because the precipitates are too small and in low volumetric amounts or dissolved in austenite during the process and did not have sufficient time to precipitate because of the high cooling rates inherent to LMD. NiAl precipitates can be up to 7 nm in diameter [24]. It should be noted that the formation of copper precipitates along the grain boundaries during the deposition of as-built 17–4 PH stainless steel via LMD has been reported [68]. Additionally, beyond the dendritic solidified region, the laser-deposited structure exhibits a fine cellular grain structure, as shown in Fig. 8. This transformation is attributed to the temperature gradient and solidification rate values. A higher temperature gradient favors the formation of cellular grains, while higher solidification rates promote dendritic morphology.

The graph also shows that the SDAS is higher for the last pass than for the first pass, indicating a more columnar and directional growth of the grains in the last pass. This is because the last pass experiences the high thermal. The relationship between the SDAS and the energy density is important for understanding the microstructure and properties of the additively manufactured parts. The SDAS can affect the anisotropy, texture, and mechanical properties of the parts, as discussed in Sect. 3.4. Therefore, it is important to carefully select and optimize the energy density and other process parameters to achieve the desired SDAS and microstructure of the parts. gradients and cooling rates, which can promote the formation of columnar grains.

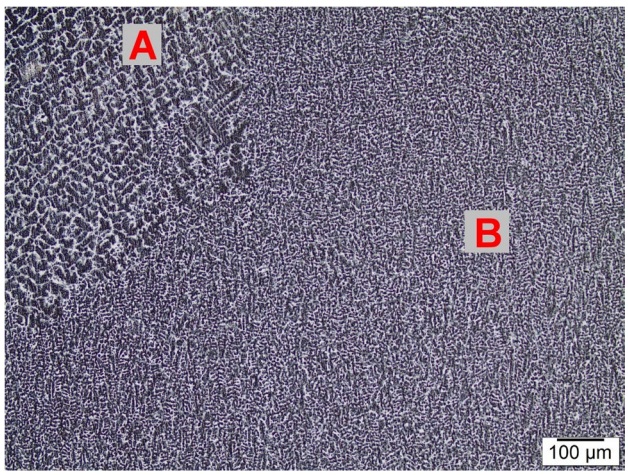

Fig. 8 Transition area of dendritic solidification (**A**) and cellular-grained structure (**B**) in the top layer. During the LMD process, heat dissipates primarily through the substrate or previously deposited layers, with some heat dissipating through the neighboring solidified layer. The cooling rate and solidification velocity at the bottom layer are very high, resulting in a progressive decrease in the cooling rate as the height of the deposit increases. This decrease in cooling rate leads to an increase in the secondary dendritic arm spacing (SDAS). Figure 9 in section shows the relationship between the secondary dendrite arm spacing (SDAS) and the energy density for the first pass and the last pass of the additively manufactured parts. The graph shows that the SDAS increases with increasing energy density, indicating a coarser and more columnar grain structure at higher energy densities. This is consistent with the optical microscopy analysis presented in Sect. 3.3, which showed that the grain size and morphology varied with the energy density and powder deposition density

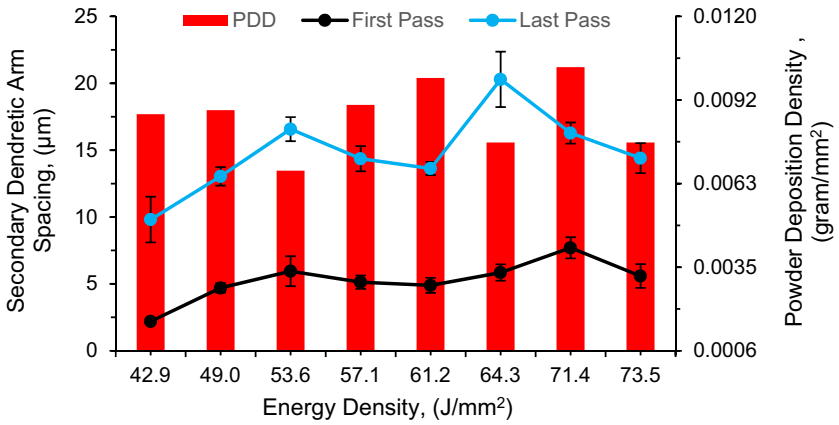

Fig. 9 Secondary dendrite arm spacing the first pass and the last pass vs. energy density

Table 3 The average Vickers hardness in different layers of the walls

Layer Number	Average Hardness (HV)
1	390.89 ± 14.61
2	393.30 ± 29.33
3	345.44 ± 18.36
4	324.47 ± 13.45
5	320.13 ± 18.32
6	312.53 ± 9.21
7	311.59 ± 13.10
8	327.19 ± 17.83
9	320.36 ± 10.15

3.4 Mechanical property evaluation

The variation in hardness values with the layer number, wall number, energy density, and powder deposition density is important for understanding the microstructure and properties of the additively manufactured parts. The hardness values can affect the wear resistance, fatigue resistance, and other mechanical properties of the parts, as well as their suitability for different applications. Therefore, it is important to carefully select and optimize the energy density, powder deposition density, and other process parameters to achieve the desired hardness values and microstructure of the parts. The results of the micro hardness test showed that the hardness of the parts varied with the energy density and powder deposition density, with the highest hardness occurring at the highest energy density and the lowest powder deposition density. The hardness also varied with the distance from the build plate, with the highest hardness occurring at the top surface and decreasing toward the bottom. The micro hardness results were consistent with the grain structure and porosity results presented in Sect. 3.3. Table 3 shows the average Vickers hardness in different layers for the straight walls. The hardness values range from 311.59 ± 13.10 HV in layer 7 to 393.30 ± 29.33 HV in layer 2. The highest hardness value is almost 27% higher than the lowest hardness value, indicating a significant variation in hardness values with the layer number. The average hardness for the walls ranges from 331 to 354 HV for a wide variation in ED/PDD. It is slightly higher than the as-built PH 13–8 Mo part (336 ± 8 HV) [18] fabricated via wire arc additive manufacturing and the as-built additively manufactured stainless steel CX part (332 ± 10 HV) [69] manufactured via laser powder bed fusion. The hardness of the PH 13–8 Mo stainless steel can be increased by subjecting them to solutionizing and aging heat treatment due to the precipitation of NiAl precipitates [42].

Figure 10 illustrates how the average Vickers hardness changes in each layer for each of the straight walls. The graph shows that the hardness values vary with the energy density and powder deposition density. For example, at an ED of 71.4 J/mm^3 and a PDD of 0.0103 g/mm^3, the hardness values range from 372.53 ± 9.21 HV in layer 2 of wall 4 to 428.30 ± 29.33 HV in layer 2 of wall 9 at an ED of 64.3 J/mm^3 and a PD 0.0077 g/mm^3. These results indicate that the energy density and powder deposition density can have a significant impact on the hardness values and microstructure of the parts. Furthermore, it was observed that there was a significant 43% increase in hardness between the second layer (420 ± 21.82 HV) and the fifth layer (295 ± 18.45 HV) in wall seven, despite having the same ED and PDD ratios. This high value in hardness in the initial layers can be attributed to rapid cooling caused by the high thermal gradient. As the number of layers increases, the thermal gradient becomes less pronounced, resulting in a decrease in the cooling rate and subsequently a decrease in hardness. In slower cooling conditions, grains have more time to grow before solidification is complete. Larger grains generally result in a coarser microstructure as discussed in Sect. 3.3. Additionally, the impact on material hardness, as mentioned, is significant. Larger grains often lead to a softer material due to the increased grain boundary area, affecting the overall mechanical properties. The relationship between build

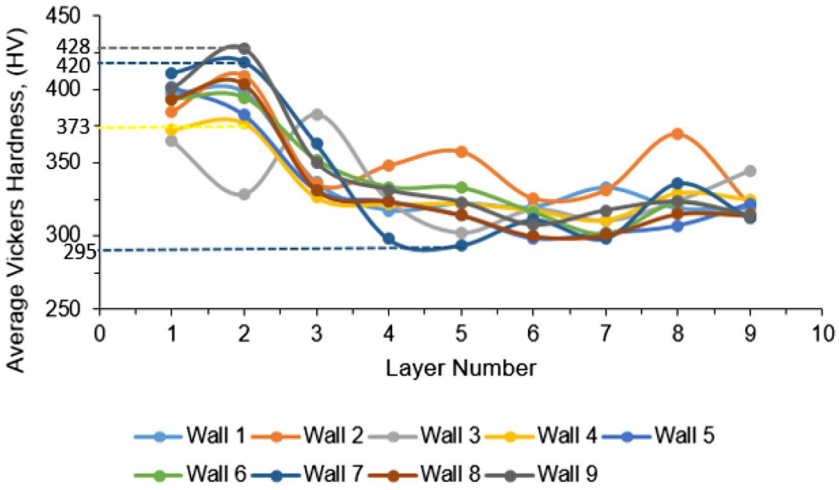

Fig. 10 Average Vickers hardness in each layer of each wall

Table 4 As-built horizontal tensile sample results extracted at different locations

Specimen number	Yield strength (MPa)	Ultimate tensile strength (MPa)	Elongation (%)
A	744.79	1129.67	6.94
B	787.29	1182.12	7.28
C	641.00	1133.78	5.17
Average	724.3 ± 75	1148.5 ± 29	6.4 ± 1.1

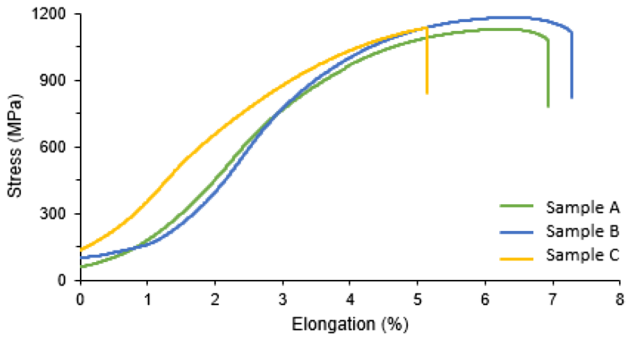

Fig. 11 Stress–strain curves of the as-printed tensile coupons in the horizontal direction at different heights

height, cooling ratio, grain size, and material hardness is a critical consideration in optimizing the manufacturing process for desired material properties. This phenomenon highlights the influence of layer height and cooling dynamics on the material properties during the additive manufacturing process.

Table 3 and Fig. 10 show a slight increase in the average Vickers hardness in the initial layers of the straight walls. This can be due to an increased cooling rate due to proximity to the substrate.

The tensile test conducted on the sample produced with an ED value is 53.57 J/mm^3 and a PDD ratio is 0.0067 g/mm^3, and three tensile samples were extracted from different locations. The resulting test data is presented in Table 4. For better visualization, Fig. 11 shows the stress elongation curve.

Minor variations are observed in the yield strength, ultimate tensile strength, and % elongation for the test coupons extracted at different locations. This can be attributed to the thermal gradient that occurred at different rates in different regions at different locations. The cooling rate varies because the substrate acts like a heat sink, interlayer dwell time and heat accumulation in the deposit as successive layers are deposited [70]. While the yield and fracture properties of these three different samples were very close to each other, the elongation amount of sample C was slightly lower, and it was assumed that porosity and other impurities might cause this. The average yield strength, determined to be 724.3 MPa, showcases the ability of the samples to resist deformation before experiencing plastic flow. Additionally, the average ultimate tensile strength of 1148.5 MPa reflects the maximum stress these samples can withstand before failure. Lastly, the average elongation of 6.4% demonstrates the extent to which the samples can stretch or deform before breaking. These average values provide valuable insights into the mechanical behavior of the samples, highlighting their strength and ductility characteristics. For PH 13–8 Mo stainless steel horizontal as-built samples fabricated via wire arc additive manufacturing technique, [70] reported average ultimate tensile strength (UTS) of 1115 ± 17 MPa and percentage elongation of 11.4 ± 1.8%. In comparison, laser-deposited horizontal as-built PH 13–8 Mo has a slightly higher average UTS, but the average % elongation is lower, as seen in Table 4. For the stainless steel CX horizontal as-built sample fabricated via laser powder bed fusion, the authors reported yield strength of (1036 MPa), UTS of 1113 MPa, and % elongation of 21.7% [42]. In comparison, laser-deposited horizontal as-built PH 13–8 Mo has

higher UTS with lower yield strength and % elongation (see Table 4). For 17–4 PH horizontal as-built sample fabricated via laser metal deposition, Yu et al. reported yield strength of 758 ± 19 MPa, UTS of 1129 ± 5 MPa, and % elongation of 14.1 ± 0.3% [28]. In comparison, laser-deposited as-built PH 13–8 Mo has higher UTS with lower yield strength and % elongation (see Table 4).

4 Conclusions

PH 13–8 Mo is a martensitic stainless steel widely used in various industries due to its high strength, toughness, and corrosion resistance. In this research, we employed the laser metal deposition process to manufacture PH 13–8 Mo martensitic stainless steel parts, including single-track thin walls and blocks. The findings from our study, encompassing microstructural analysis, hardness measurements, and uniaxial tensile tests of the additively manufactured parts, can be summarized as follows:

The geometry of straight walls is significantly influenced by the energy density and powder deposition density. Central wall height ranges from 6.56 to 11.96 mm, while the width ranges from 3.97 to 5.00 mm. The first layer penetration below the substrate varies from 77.53 to 307.5 µm, exhibiting a wide range of energy density and powder deposition density.

Analysis of cross-sectional porosity in straight walls revealed that the pore diameter, resulting from entrapped gas, increases from 15.61 to 54.19 µm. Simultaneously, the maximum gap length due to lack of fusion decreases from 174.34 to 28.27 µm with an increase in energy density.

Columnar dendrites constitute the primary grain morphology in the microstructure of straight walls. The secondary dendritic arm spacing (SDAS) increases with the height of the straight walls. SDAS ranges from 2.2 to 7.7 µm in the first layer and from 7.61 to 14.44 µm in the top layer.

The average Vickers hardness ranges from 331 to 354 HV, reflecting the wide variation in energy density and powder deposition density. Notably, higher hardness is observed in layers close to the substrate due to the heat sink effect.

The uniaxial tensile tests conducted on horizontal tensile specimens demonstrated that the ultimate tensile strength (UTS) of laser-deposited PH 13–8 Mo (~ 1148.5 MPa) was comparable to that of WAAM PH 13–8 Mo parts (~ 1117 MPa), L-PBF-built CX stainless steel parts (~ 1113 MPa), and laser-deposited 17–4 PH parts (~ 1129 MPa).

These results indicate the feasibility and effectiveness of utilizing the LMD process to fabricate PH 13–8 Mo martensitic stainless steel parts with desirable mechanical properties. The findings provide valuable insights for further optimizing the manufacturing parameters and enhancing the performance of additively manufactured PH 13–8 Mo components in diverse applications.

Author contribution statement Mustafa Kas: conceptualization, methodology, and writing—review and editing. Talha Muslim: conceptualization, methodology, investigation, writing—original draft, writing—review and editing, and visualization. Oguzhan Yilmaz: conceptualization, methodology, writing—review and editing, and supervision. Taner Karagöz: conceptualization, methodology, and writing—review and editing. Enbiya Turedi: investigation, data curation, and writing—review and editing. Serap Gumus: investigation, data curation, and writing—review and editing. Alperen Bayram: project administration and funding acquisition.

Funding Open access funding provided by the Scientific and Technological Research Council of Türkiye (TÜBİTAK). This work was supported by TUBITAK and Coşkunöz Holding (2244 Industrial Doctorate Program no. 119C059) and by TUBITAK, Eureka, Eureka Smart Cluster and Coşkunöz Holding (grant agreement no. 9190007).

Declarations

Competing interests The authors declare no competing interests.

Open Access This article is licensed under a Creative Commons Attribution 4.0 International License, which permits use, sharing, adaptation, distribution and reproduction in any medium or format, as long as you give appropriate credit to the original author(s) and the source, provide a link to the Creative Commons licence, and indicate if changes were made. The images or other third party material in this article are included in the article's Creative Commons licence, unless indicated otherwise in a credit line to the material. If material is not included in the article's Creative Commons licence and your intended use is not permitted by statutory regulation or exceeds the permitted use, you will need to obtain permission directly from the copyright holder. To view a copy of this licence, visit http://creativecommons.org/licenses/by/4.0/.

References

1. Oh WJ, Son Y, Cho SY et al (2020) Solution annealing and precipitation hardening effect on the mechanical properties of 630 stainless steel fabricated via laser melting deposition. Mater Sci Eng A 794:139999. https://doi.org/10.1016/J.MSEA.2020.139999
2. Akbari M, Kovacevic R (2018) An investigation on mechanical and microstructural properties of 316LSi parts fabricated by a robotized laser/wire direct metal deposition system. Addit Manuf 23:487–497. https://doi.org/10.1016/J.ADDMA.2018.08.031
3. Chen Y, Chen X, Jiang M et al (2022) Coaxial laser metal wire deposition of Ti6Al4V alloy: process, microstructure and mechanical properties. J Mater Res Technol 20:2578–2590. https://doi.org/10.1016/j.jmrt.2022.08.068
4. Zhang X, Li W, Chen X et al (2018) Evaluation of component repair using direct metal deposition from scanned data. Int J Adv Manuf Technol 95:3335–3348. https://doi.org/10.1007/s00170-017-1455-y
5. Pan T, Zhang X, Yamazaki T et al (2020) Characteristics of Inconel 625—copper bimetallic structure fabricated by directed energy deposition. Int J Adv Manuf Technol 109:1261–1274. https://doi.org/10.1007/s00170-020-05713-z
6. Yadav S, Jinoop AN, Sinha N et al (2020) Parametric investigation and characterization of laser directed energy deposited

copper-nickel graded layers. Int J Adv Manuf Technol 108:3779–3791. https://doi.org/10.1007/s00170-020-05644-9
7. Li B, Zhang R, Malik A, Li W (2022) Machinability of partition milling stainless steel/Inconel functionally gradient material printed with directed energy deposition. Int J Adv Manuf Technol 122:3009–3022. https://doi.org/10.1007/s00170-022-10111-8
8. Riveiro A, del Val J, Comesaña R et al (2019) Laser additive manufacturing processes for near net shape components. Springer, Cham, pp 105–141
9. Piscopo G, Iuliano L (2022) Current research and industrial application of laser powder directed energy deposition. Int J Adv Manuf Technol 119:6893–6917
10. Hama-Saleh R, Yildirim K, Hemes S et al (2021) Investigation of high-depostition-rate additive manufacturing of Ti-6Al-4V via laser material deposition. In: ESAFORM 2021 - 24th International Conference on Material Forming. Prof. Anne Marie Habraken
11. Mazzucato F, Forni D, Valente A, Cadoni E (2021) Laser metal deposition of Inconel 718 alloy and as-built mechanical properties compared to casting. Materials (Basel) 14:1–21. https://doi.org/10.3390/ma14020437
12. Langebeck A, Bohlen A, Rentsch R, Vollertsen F (2021) Low-defect AM of high strength aluminium alloy by LMD. SSRN Electron J. https://doi.org/10.2139/SSRN.3785871
13. Yang SF, Li CW, Chen AY et al (2021) Microstructure and corrosion resistance of stainless steel manufactured by laser melting deposition. J Manuf Process 65:418–427. https://doi.org/10.1016/j.jmapro.2021.03.051
14. Siva Prasad H, Brueckner F, Volpp J, Kaplan AFH (2020) Laser metal deposition of copper on diverse metals using green laser sources. Int J Adv Manuf Technol 107:1559–1568. https://doi.org/10.1007/S00170-020-05117-Z/TABLES/4
15. Alım B, Özpolat ÖF, Şakar E et al (2022) Precipitation-hardening stainless steels: potential use radiation shielding materials. Radiat Phys Chem 194:110009. https://doi.org/10.1016/j.radphyschem.2022.110009
16. Bahrami Balajaddeh M, Naffakh-Moosavy H (2019) Pulsed Nd:YAG laser welding of 17–4 PH stainless steel: microstructure, mechanical properties, and weldability investigation. Opt Laser Technol 119:105651. https://doi.org/10.1016/J.OPTLASTEC.2019.105651
17. Das CR, Dey HC, Srinivasan G et al (2006) Weldability of 17–4PH stainless steel in overaged heat treated condition. Sci Technol Weld Join 11:502–508. https://doi.org/10.1179/174329306X148147
18. Lippold JC, Kotecki DJ (2005) Welding metallurgy and weldability of stainless steels, p 376
19. Vander Voort GF, Lucas GM, Manilova EP (2004) Metallography and microstructures of stainless steels and maraging steels. Metallogr Microstruct 670–700. https://doi.org/10.31399/ASM.HB.V09.A0003767
20. Schnitzer R, Radis R, Nöhrer M et al (2010) Reverted austenite in PH 13–8 Mo maraging steels. Mater Chem Phys 122:138–145. https://doi.org/10.1016/j.matchemphys.2010.02.058
21. Ghaffari M, Vahedi Nemani A, Nasiri A (2022) Microstructure and mechanical behavior of PH 13–8Mo martensitic stainless steel fabricated by wire arc additive manufacturing. Addit Manuf 49:. https://doi.org/10.1016/j.addma.2021.102374
22. Tsay LW, Chen HH, Chiang MF, Chen C (2007) The influence of aging treatments on sulfide stress corrosion cracking of PH 13–8 Mo steel welds. Corros Sci 49:2461–2473. https://doi.org/10.1016/j.corsci.2006.12.006
23. Zheng B, Smugeresky JE, Zhou Y, Lavernia EJ (2006) Microstructure and properties of PH13–8Mo steel fabricated by LENS. https://doi.org/10.2172/10142257
24. Seetharaman V, Sundararaman M, Krishnan R (1981) Precipitation hardening in a PH 13–8 Mo stainless steel. Mater Sci Eng 47:1–11. https://doi.org/10.1016/0025-5416(81)90034-3
25. Zai L, Zhang C, Wang Y et al (2020) Laser powder bed fusion of precipitation-hardened martensitic stainless steels: a review. Metals 255(10):255. https://doi.org/10.3390/MET10020255
26. Adeyemi AA, Akinlabi E, Mahamood RM et al (2017) Influence of laser power on microstructure of laser metal deposited 17–4 ph stainless steel. IOP Conf Ser Mater Sci Eng 225:012028. https://doi.org/10.1088/1757-899x/225/1/012028
27. Vendra LJ, Achanta A, Sullivan E (2020) Fatigue behavior of laser metal deposited 17–4 PH stainless steel. In: ASTM Special Technical Publication. pp 399–414
28. Yu Z, Zheng Y, Chen J, et al (2020) Effect of laser remelting processing on microstructure and mechanical properties of 17–4 PH stainless steel during laser direct metal deposition. J Mater Process Technol 284:. https://doi.org/10.1016/j.jmatprotec.2020.116738
29. Caballero A, Ding J, Ganguly S, Williams S (2019) Wire + Arc additive manufacture of 17–4 PH stainless steel: effect of different processing conditions on microstructure, hardness, and tensile strength. J Mater Process Technol 268:54–62. https://doi.org/10.1016/j.jmatprotec.2019.01.007
30. Martina F, Ding J, Williams S et al (2019) Tandem metal inert gas process for high productivity wire arc additive manufacturing in stainless steel. Addit Manuf 25:545–550. https://doi.org/10.1016/J.ADDMA.2018.11.022
31. AlMangour B, Yang JM (2016) Improving the surface quality and mechanical properties by shot-peening of 17–4 stainless steel fabricated by additive manufacturing. Mater Des 110:914–924. https://doi.org/10.1016/j.matdes.2016.08.037
32. AlMangour B, Yang JM (2017) Integration of heat treatment with shot peening of 17–4 stainless steel fabricated by direct metal laser sintering. JOM 69:2309–2313. https://doi.org/10.1007/S11837-017-2538-9/FIGURES/4
33. Averyanova M, Cicala E, Bertrand P, Grevey D (2012) Experimental design approach to optimize selective laser melting of martensitic 17–4 PH powder: part i - single laser tracks and first layer. Rapid Prototyp J 18:28–37. https://doi.org/10.1108/13552541211193476/FULL/PDF
34. Hu Z, Zhu H, Zhang H, Zeng X (2017) Experimental investigation on selective laser melting of 17–4PH stainless steel. Opt Laser Technol 87:17–25. https://doi.org/10.1016/J.OPTLASTEC.2016.07.012
35. Murr LE, Martinez E, Hernandez J et al (2012) Microstructures and properties of 17–4 PH stainless steel fabricated by selective laser melting. J Mater Res Technol 1:167–177. https://doi.org/10.1016/S2238-7854(12)70029-7
36. Wang D, Chi CT, Wang WQ et al (2019) The effects of fabrication atmosphere condition on the microstructural and mechanical properties of laser direct manufactured stainless steel 17–4 PH. J Mater Sci Technol 35:1315–1322. https://doi.org/10.1016/J.JMST.2019.03.009
37. Aripin MA, Sajuri Z, Jamadon NH et al (2023) Microstructure and mechanical properties of selective laser melted 17–4 PH stainless steel; build direction and heat treatment processes. Mater Today Commun 36:106479. https://doi.org/10.1016/j.mtcomm.2023.106479
38. AlMangour B, Yang JM (2017) Understanding the deformation behavior of 17–4 precipitate hardenable stainless steel produced by direct metal laser sintering using micropillar compression and TEM. Int J Adv Manuf Technol 90:119–126. https://doi.org/10.1007/s00170-016-9367-9
39. Sanjari M, Hadadzadeh A, Pirgazi H et al (2020) Selective laser melted stainless steel CX: role of built orientation on

microstructure and micro-mechanical properties. Mater Sci Eng A 786:139365. https://doi.org/10.1016/j.msea.2020.139365
40. Turnier Trottier W, Kreitcberg A, Brailovski V (2021) Structure and mechanical properties of laser powder bed-fused and wrought ph13-8mo-type precipitation hardening stainless steels: comparative study. J Manuf Mater Process 5:67. https://doi.org/10.3390/jmmp5030067
41. Zhang J, Wang M, Niu L et al (2021) Effect of process parameters and heat treatment on the properties of stainless steel CX fabricated by selective laser melting. J Alloys Compd 877:160062. https://doi.org/10.1016/j.jallcom.2021.160062
42. Asgari H, Mohammadi M (2018) Microstructure and mechanical properties of stainless steel CX manufactured by direct metal laser sintering. Mater Sci Eng A 709:82–89. https://doi.org/10.1016/J.MSEA.2017.10.045
43. Vahedi Nemani A, Ghaffari M, Salahi S, Nasiri A (2023) On the microstructural characteristics and corrosion performance of as-printed and heat-treated PH 13–8Mo martensitic stainless steel fabricated by wire arc additive manufacturing. Mater Today Commun 34:105477. https://doi.org/10.1016/j.mtcomm.2023.105477
44. Muslim T, Karagoz T, Ozkok R et al (2021) Influence of laser energy density on geometrical forms produced by laser metal deposition of PH 13–8 Mo stainless steel. J Addit Manuf Technol 1:591. https://doi.org/10.18416/JAMTECH.2111591
45. Kim MJ, Saldana C (2023) Post-processing of additively manufactured IN625 thin-walled structures using laser remelting in directed energy deposition. J Manuf Process 88:59–70. https://doi.org/10.1016/j.jmapro.2022.12.053
46. Mahamood RM, (2018) Laser metal deposition process of metals, alloys, and composite materials. Engineering Materials and Processes 119–141.Springer International Publishing, Cham https://doi.org/10.1007/978-3-319-649
47. Mahamood RM, Akinlabi ET, Shukla M, Pityana S (2012) Effect of laser power on material efficiency, layer height and width of laser metal deposited Ti6Al4V. In: Lecture Notes in Engineering and Computer Science. pp 1433–1438
48. Li Y, Yang H, Lin X et al (2003) The influences of processing parameters on forming characterizations during laser rapid forming. Mater Sci Eng A 360:18–25. https://doi.org/10.1016/S0921-5093(03)00435-0
49. Wang L, Pratt P, Felicelli SD, et al (2009) Experimental analysis of porosity formation in laser-assisted powder deposition process. In: TMS Annual Meeting. pp 389–396
50. Mahamood RM, Akinlabi ET, Shukla M, Pityana S (2014) Characterizing the effect of processing parameters on the porosity of laser deposited titanium alloy powder. In: Lecture Notes in Engineering and Computer Science
51. Jiang M, Mukherjee T, Du Y, DebRoy T (2022) Superior printed parts using history and augmented machine learning. npj Comput Mater 8:1–10. https://doi.org/10.1038/s41524-022-00866-9
52. Coeck S, Bisht M, Plas J, Verbist F (2019) Prediction of lack of fusion porosity in selective laser melting based on melt pool monitoring data. Addit Manuf 25:347–356. https://doi.org/10.1016/j.addma.2018.11.015
53. Susan DF, Puskar JD, Brooks JA, Robino CV (2006) Quantitative characterization of porosity in stainless steel LENS powders and deposits. Mater Charact 57:36–43. https://doi.org/10.1016/j.matchar.2005.12.005
54. Ahsan MN, Bradley R, Pinkerton AJ (2011) Microcomputed tomography analysis of intralayer porosity generation in laser direct metal deposition and its causes. J Laser Appl 23:022009. https://doi.org/10.2351/1.3582311
55. Lin PY, Shen FC, Wu KT et al (2020) Process optimization for directed energy deposition of SS316L components. Int J Adv Manuf Technol 111:1387–1400. https://doi.org/10.1007/s00170-020-06113-z
56. Liu M, Kumar A, Bukkapatnam S, Kuttolamadom M (2021) A review of the anomalies in directed energy deposition (DED) processes & potential solutions - part quality & defects. In: Procedia Manufacturing. Elsevier, pp 507–518
57. Bax B, Rajput R, Kellet R, Reisacher M (2018) Systematic evaluation of process parameter maps for laser cladding and directed energy deposition. Addit Manuf 21:487–494. https://doi.org/10.1016/j.addma.2018.04.002
58. Young NO, Goldstein JS, Block MJ (1959) The motion of bubbles in a vertical temperature gradient. J Fluid Mech 6:350–356. https://doi.org/10.1017/S0022112059000684
59. Ratna Y (2017) The effect of thermal history during additive manufacturing on the microstructure and hardness of H13 steel
60. Ng GKL, Jarfors AEW, Bi G, Zheng HY (2009) Porosity formation and gas bubble retention in laser metal deposition. Appl Phys A Mater Sci Process 97:641–649. https://doi.org/10.1007/s00339-009-5266-3
61. Kuriya T, Koike R, Mori T, Kakinuma Y (2018) Relationship between solidification time and porosity with directed energy deposition of Inconel 718. J Adv Mech Des Syst Manuf 12:JAMDSM0104. https://doi.org/10.1299/jamdsm.2018jamdsm0104
62. Cui N, Kong F, Wang X et al (2016) Microstructural evolution, hot workability, and mechanical properties of Ti-43Al-2Cr-2Mn-0.2Y alloy. Mater Des 89:1020–1027. https://doi.org/10.1016/j.matdes.2015.10.076
63. Brody HD (1986) Segregation and structure in the weld zone. In: Advances in welding science and technology. TWR '86. Proceedings of an international conference on trends in welding research. ASM International, Gatlinburg, Tennessee, USA, pp 83–91
64. Eghlimi A, Shamanian M, Eskandarian M et al (2015) Evaluation of microstructure and texture across the welded interface of super duplex stainless steel and high strength low alloy steel. Surf Coatings Technol 264:150–162. https://doi.org/10.1016/j.surfcoat.2014.12.060
65. Cieslak MJ, Hills CR, Hlava PF, David SA (1990) An investigation of the high-temperature and solidification microstructures of PH 13–8 Mo stainless steel. Metall Trans A 21:2465–2475. https://doi.org/10.1007/BF02646991
66. Brooks JA, Garrison, Jr WR (1999) Weld microstructure development and properties of precipitation-strengthened martensitic stainless steels. Weld J (Miami, Fla) 78:
67. Chen X, Li J, Cheng X et al (2017) Microstructure and mechanical properties of the austenitic stainless steel 316L fabricated by gas metal arc additive manufacturing. Mater Sci Eng A 703:567–577. https://doi.org/10.1016/j.msea.2017.05.024
68. Mathoho I, Akinlabi ET, Arthur N, Tlotleng M (2020) Impact of DED process parameters on the metallurgical characteristics of 17–4 PH SS deposited using DED. CIRP J Manuf Sci Technol 31:450–458. https://doi.org/10.1016/j.cirpj.2020.07.007
69. Hadadzadeh A, Shahriari A, Amirkhiz BS et al (2020) Additive manufacturing of an Fe–Cr–Ni–Al maraging stainless steel: microstructure evolution, heat treatment, and strengthening mechanisms. Mater Sci Eng A 787:139470. https://doi.org/10.1016/j.msea.2020.139470
70. Ghaffari M, Vahedi Nemani A, Nasiri A (2022) Microstructure and mechanical behavior of PH 13–8Mo martensitic stainless steel fabricated by wire arc additive manufacturing. Addit Manuf 49:102374. https://doi.org/10.1016/j.addma.2021.102374

Publisher's Note Springer Nature remains neutral with regard to jurisdictional claims in published maps and institutional affiliations.